Electronically Induced Atom Motion in Engineered CoCu n Nanostructures

Joseph A. Stroscio, *et al.*

Science **313**, 948 (2006);
DOI: 10.1126/science.1129788

A9 and A10, and showed 16-nm periodicity [Fig. 4, B, D, and I; pink dot in Fig. 4 (E and F) and Fig. 5C]. MIP3 was the largest and lay between protofilaments B9 and B10 with 16 nm-periodicity [Fig. 4, C, D, and I; red dot in Fig. 4, E and F, and Fig. 5C]. The MIPs were present in all outer doublets and in both sea urchin (Fig. 4, G to I) and *Chlamydomonas* (Fig. 4, A to F), suggesting that they are universal features of axonemes. Although material has previously been seen in the lumen of doublets from insect and human sperm (*29*), MIPs have not been recognized as a consistent, periodic feature of outer doublets. Images of homogenized, high salt–extracted sea urchin sperm flagella also revealed features inside doublet MTs (*30*), but this study was limited by nonphysiological conditions and by the anisotropic resolution that is characteristic of single-axis tomography (fig. S1).

Doublet MTs treated with increasing concentrations of ionic detergents dissolve in a defined sequence: first the outer portion of the B tubule, then the rest of the B tubule, followed by the outer portion of the A tubule and then the remainder of the A tubule, leaving a ribbon of three protofilaments (*31*). Our axonemes were incubated in physiological buffers, but occasionally they contained a few partially dissolved doublets that were consistent with this pattern of disintegration. In one example, the A tubule was intact, but only protofilaments B9 to B11 remained; these still bound MIP3 (Fig. 4, J and K), suggesting that MIPs give structural stability to MTs protofilaments. Several small ligands, such as Taxol, interact with the luminal side of the MT wall and affect polymer stability (*32*). Perhaps MIPs alter doublet stability in a similar way. Doublet stability may also be affected by the especially robust ribbon of three protofilaments that include tubulin, tektin, and several tightly associated proteins (*28*). Tektin may also associate with the DRC and IDAs (*33*). Notably, MIP1 was in the A tubule close to the DRC, and MIP3 was in the B tubule near the attachment of nexin (Fig. 5C). Perhaps the MIPs provide structural reinforcement at sites of mechanical stress and information transfer. The further characterization of these proteins may provide valuable physiological and therapeutic insights.

Future comparisons between wild-type and mutant axonemes should help to define the function of additional components in the axoneme. Work on mutant axonemes from human patients may also help to clarify the underlying causes of diseases related to flagellar and ciliary dysfunction. Given the complexity of axoneme structure and the biological importance of its many functions, cryo-ET is likely to play a major role in clarifying both the normal and abnormal mechanisms of this conserved biological machine.

References and Notes

1. M. E. Porter, W. S. Sale, *J. Cell Biol.* **151**, F37 (2000).
2. E. F. Smith, P. Yang, *Cell Motil. Cytoskeleton* **57**, 8 (2004).
3. J. Pan, Q. Wang, W. J. Snell, *Lab. Invest.* **85**, 452 (2005).
4. G. B. Witman, J. Plummer, G. Sander, *J. Cell Biol.* **76**, 729 (1978).
5. M. Sakato, S. M. King, *J. Struct. Biol.* **146**, 58 (2004).
6. U. W. Goodenough, J. E. Heuser, *Structure of the Soluble and in Situ Ciliary Dyneins Visualized by Quick-Freeze Deep-Etch Microscopy,* vol. 1 of *Cell Movement*, F. P. Warner, Ed. (Liss, New York, 1989).
7. I. R. Gibbons, *J. Cell Biol.* **91**, 107s (1981).
8. P. Lupetti *et al.*, *Cell Motil. Cytoskeleton* **62**, 69 (2005).
9. Materials and methods are available as supporting material on *Science* Online.
10. J. Frank, *Electron Tomography: Three-Dimensional Imaging with the Transmission Electron Microscope* (Plenum, New York, 1992).
11. A. J. Koster *et al.*, *J. Struct. Biol.* **120**, 276 (1997).
12. D. Nicastro, J. R. McIntosh, W. Baumeister, *Proc. Natl. Acad. Sci. U.S.A.* **102**, 15889 (2005).
13. S. A. Burgess, M. L. Walker, H. Sakakibara, P. J. Knight, K. Oiwa, *Nature* **421**, 715 (2003).
14. M. P. Koonce, M. Samso, *Trends Cell Biol.* **14**, 612 (2004).
15. H. Sakakibara, S. Takada, S. M. King, G. B. Witman, R. Kamiya, *J. Cell Biol.* **122**, 653 (1993).
16. S. Takada, R. Kamiya, *J. Cell Biol.* **126**, 737 (1994).
17. S. A. Burgess, P. J. Knight, *Curr. Opin. Struct. Biol.* **14**, 138 (2004).
18. S. A. Burgess, S. D. Dover, D. M. Woolley, *J. Cell Sci.* **98**, 17 (1991).
19. G. B. Witman, N. Minervini, *Symp. Soc. Exp. Biol.* **35**, 203 (1982).
20. D. N. Mastronarde, E. T. O'Toole, K. L. McDonald, J. R. McIntosh, M. E. Porter, *J. Cell Biol.* **118**, 1145 (1992).
21. L. C. Gardner, E. O'Toole, C. A. Perrone, T. Giddings, M. E. Porter, *J. Cell Biol.* **127**, 1311 (1994).
22. R. Kamiya, *Int. Rev. Cytol.* **219**, 115 (2002).
23. S. H. Myster, J. A. Knott, E. O'Toole, M. E. Porter, *Mol. Biol. Cell* **8**, 607 (1997).
24. L. M. DiBella *et al.*, *Mol. Biol. Cell* **15**, 4633 (2004).
25. G. Piperno, K. Mead, M. LeDizet, A. Moscatelli, *J. Cell Biol.* **125**, 1109 (1994).
26. D. M. Woolley, *J. Cell Sci.* **110**, 85 (1997).
27. C. B. Lindemann, L. J. Macauley, K. A. Lesich, *Biophys. J.* **89**, 1165 (2005).
28. D. Nojima, R. W. Linck, E. H. Egelman, *Curr. Biol.* **5**, 158 (1995).
29. B. A. Afzelius, R. Dallai, S. Lanzavecchia, P. L. Bellon, *Tissue Cell* **27**, 241 (1995).
30. H. Sui, K. H. Downing, *Nature*, **442**, 475 (2006).
31. G. B. Witman, K. Carlson, J. Berliner, J. L. Rosenbaum, *J. Cell Biol.* **54**, 507 (1972).
32. K. H. Downing, *Annu. Rev. Cell Dev. Biol.* **16**, 89 (2000).
33. H. A. Yanagisawa, R. Kamiya, *Mol. Biol. Cell* **15**, 2105 (2004).

34. We thank R. Linck for helpful discussions, D. Mastronarde for help with image processing, and the National Center for Research Resources (grant RR 000592 to J.R.M.) and NIH (grant 2R37-GM55667 to M.E.P.) for financial support.

Supporting Online Material

www.sciencemag.org/cgi/content/full/313/5789/944/DC1
Materials and Methods
SOM Text
Figs. S1 to S4
References
Movies S1 to S6

11 April 2006; accepted 5 July 2006
10.1126/science.1128618

REPORTS

Electronically Induced Atom Motion in Engineered $CoCu_n$ Nanostructures

Joseph A. Stroscio,[1]* Francesca Tavazza,[2] Jason N. Crain,[1] Robert J. Celotta,[1] Anne M. Chaka[2]

We have measured the quantum yield for exciting the motion of a single Co atom in $CoCu_n$ linear molecules constructed on a Cu(111) surface. The Co atom switched between two lattice positions during electron excitation from the tip of a scanning tunneling microscope. The tip location with highest probability for inducing motion was consistent with the position of an active state identified through electronic structure calculations. Atom motion within the molecule decreased with increased molecular length and reflected the corresponding variation in electronic structure.

Atom manipulation with the scanning tunneling microscope (STM) is accomplished by using a tunable chemical bond between the adatom and the scanning tip and/or local electronic excitations via the tunneling electrons (*1*–*3*). The dynamics of atomic motion during such processes can be followed by analyzing the noise in the tunneling signal (*4*, *5*). Such atomic motion is ultimately controlled by both the energy landscape and the type of excitation and relaxation pathways the atoms encounter, as revealed by recent tunneling noise spectroscopy studies for single atoms and small molecules (*6*–*11*). Through clever design of molecular configurations, energy barriers can be engineered to facilitate long-range motion in larger molecular nanostructures (*12*).

In this report, we demonstrate that motion of a single atom within a larger nanostructure can be induced by using electron excitation mechanisms in the STM. The use of tunneling noise spectroscopy measurements, together with den-

[1]Center for Nanoscale Science and Technology, [2]Chemical Science and Technology Laboratory, National Institute of Standards and Technology, Gaithersburg, MD 20899–8412, USA.

*To whom correspondence should be addressed. E-mail: joseph.stroscio@nist.gov

sity functional calculations, allows us to study molecular stability and the energy barriers hindering atom motion, each as a function of nanostructure size. In the $CoCu_n$ linear structures we studied, we mapped the probability for inducing motion and found it is localized on the atomic scale but is not centered over the adatom whose movement is induced. These probability maps are found to be consistent with the location of a resonant state that overlaps the Fermi edge (chemically active "frontier" molecular orbitals). We also show how to use the quantum electronic structure of the linear nanostructure to "tune" the atom dynamics by changing the energy barriers for motion.

We built $CoCu_n$ linear chain nanostructures by using STM atom manipulation techniques (*1*–*3*, *13*). The construction began by bringing together two Cu atoms to form a Cu_2 dimer and then attaching a single Co atom to the dimer (fig. S1, A to C). The Co atom resides in the same face-centered cubic (fcc) site as the Cu atoms, resulting in a linear configuration (Fig. 1A). The Co atom can be induced to switch to the nearby hexagonal close-packed (hcp) site to create a canted molecular configuration (Fig. 1B). This switching occurred when inelastic electron tunneling injected energy into the Co-Cu bonds and caused vibrational excitation (fig. S1C and Fig. 1C). Noise features in the STM topograph are seen on the left side of the Co atom, corresponding to imaging the Co atom in the linear configuration (Fig. 1A) part of the time and in the canted configuration (Fig. 1B) at other times as the image is acquired. Noise features were not observed at very low tunneling biases, which produced an image of a stationary linear molecule. Low-frequency (~1 Hz) noise, on the time scale of the STM scan, was observed to begin at ~10 mV bias (Fig. 1C) and suggested an energy threshold for atom motion.

The tunneling noise associated with the Co atom in the $CoCu_2$ molecule switching between the fcc and hcp sites exhibits two-state random telegraph noise characteristics (Fig. 1D inset). Random telegraph noise is associated with an exponentially distributed residence time distribution (Fig. 1D), which is fit to yield the average residence time, τ, for the atom in a particular state. Insight into the mechanisms and energy barriers for the atom motion can be obtained from determining the atom transfer rate, $R = \tau^{-1}$, and quantum yield (probability of switching per tunneling electron), $(I\tau/e)^{-1}$, as a function of tunneling current, I, and voltage, V (*4*–*11*). For the $CoCu_2$ molecule and a tunneling bias voltage of 40 mV, the transfer rate for the Co atom from the fcc site is observed to vary as a power law in the tunneling current, I^N, where $N = 1.3 \pm 0.1$ (Fig. 2B). The near-unity value of N implies a predominantly single-electron process for switching the Co atom in the $CoCu_2$ molecule.

A clear, single voltage threshold of ~15 mV, largely independent of the initial current setpoint, was observed in the quantum yield measurements (Fig. 2A). The nearly constant quantum yield above threshold is consistent with the near-unity power-law dependence of transfer rate versus current, because the tunneling current is linear in bias voltage in this voltage range. We interpret these results by using a model where the Co atom overcomes the po-

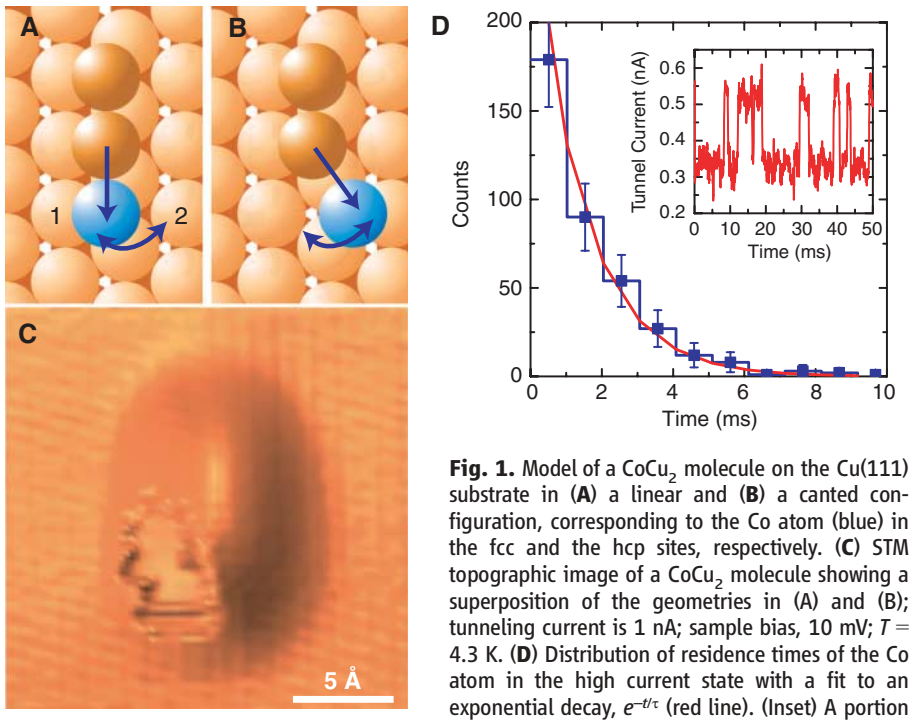

Fig. 1. Model of a $CoCu_2$ molecule on the Cu(111) substrate in (**A**) a linear and (**B**) a canted configuration, corresponding to the Co atom (blue) in the fcc and the hcp sites, respectively. (**C**) STM topographic image of a $CoCu_2$ molecule showing a superposition of the geometries in (A) and (B); tunneling current is 1 nA; sample bias, 10 mV; T = 4.3 K. (**D**) Distribution of residence times of the Co atom in the high current state with a fit to an exponential decay, $e^{-t/\tau}$ (red line). (Inset) A portion of the tunneling current–versus–time trace obtained in the left vicinity of the Co atom in the $CoCu_2$ molecule at 15.4 mV sample bias.

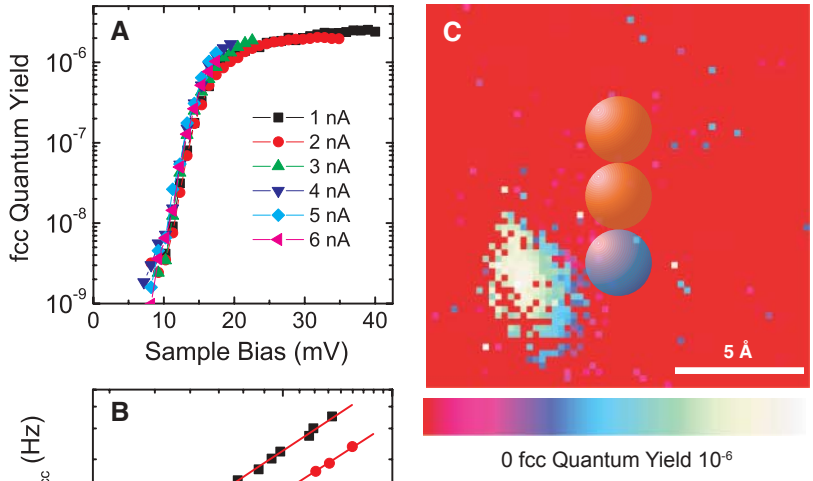

Fig. 2. (**A**) Fcc quantum yield as a function of sample bias at fixed tip-sample separation. Symbols correspond to different set-point currents for each measurement. The tip-sample separation varied by 0.75 Å when changing the current set point from 1 to 6 nA at 40 mV sample bias. (**B**) Transfer rate for the Co atom out of the fcc site as a function of tunneling current obtained at a fixed sample bias of 40 mV for the $CoCu_2$ molecule. The three curves were obtained at different locations near the Co atom and are fit to I^N (red lines). The average of the three data sets yields $N = 1.3 \pm 0.1$ (red lines). (**C**) Simultaneous spatial images of the quantum yield and STM topography (not shown) for the $CoCu_2$ molecule; sample bias, 40 mV; tunnel current, 1 nA; T = 4.3 K. Positions of the Co (blue) and Cu (gold) atoms are schematically superimposed on the quantum yield image.

tential barrier between fcc and hcp sites via an inelastic electron tunneling excitation. In the resonance tunneling model (*14*–*17*), a small fraction of electrons tunnels inelastically into a $CoCu_2$ state to create a positive- or negative-ion resonance state. While an electron is temporarily trapped in this state, the $CoCu_2$ molecular ion resides on an excited-state potential until the resonance decays on the time scale of femtoseconds and leaves the molecule in an excited vibrational state. If the electron energy is sufficient to place this excited vibrational state near the top of the potential barrier, bond breaking can occur. When the energy relaxation rate is much faster than the tunneling rate, a single-step or few-steps excitation is favored; bond breaking occurs after a minimum number of inelastic scattering events contributes a total energy sufficient to overcome the potential barrier. In this resonance tunneling model, the voltage threshold of ~15 mV corresponds to the potential barrier height for the Co atom in the $CoCu_2$ molecule to transfer between fcc and hcp sites.

We also examined the spatial distribution of the excitation probability for inducing motion. Naïvely, we might expect the probability to be centered over the atom of interest. The STM topographic image in Fig. 1C, however, shows that Co atom switching is only observed when the STM probe tip is in a certain location. More detailed measurements were made by recording the tunneling noise spectrum at each pixel along with the STM topography to obtain simultaneous atom dynamics and STM topographic data. The noise spectra at each lateral position were analyzed to obtain a spatial map of transfer rates and quantum yields for leaving the fcc and the hcp sites. The spatial map of the quantum yield (Fig. 2C) for Co atom motion for the $CoCu_2$ molecule shows that the probability for inducing motion is localized on the atomic scale and is positioned to the left of the Co atom. Density functional theory (DFT) calculations link the vibrational coupling excitation to a resonant *d* state localized on the Co atom (Fig. 3, A and C). The localized position of the quantum yield (Fig. 2C) is consistent with the calculated density of states at the Fermi level (E_F), which shows a maximum to the left of the Co atom, and demonstrates the need to inject energy into the appropriate Co-Cu substrate bond (Cu atom labeled no. 1 in Fig. 1A) to move the Co atom from the favored fcc site. This insight raises the possibility that molecular orbital analysis may be used to guide the design and the control of single-atom manipulation by STM in nanostructures.

Varying the Cu chain length affects the quantum electronic states of the molecule (*18*), in turn influencing the atom dynamics. We systematically varied the $CoCu_n$ molecular structure by building longer Cu segments. Topographic images of $CoCu_n$ molecules with *n* values from 2 to 5 display a varying degree of tunneling noise near the Co atom (Fig. 3B). The noise feature is seen to diminish with longer molecular length and is almost absent when *n* reaches 5, indicating increased stability of the Co atom in the fcc site. DFT calculations elucidate the electronic origins for this trend, focusing on a state (Fig. 3A) that is both localized near the Co atom and important at low tunneling bias voltages. Analysis of the calculated density of states shows a depletion of active Co *d* states at E_F as the molecular chain length increases. This depletion of active states at E_F is consistent with the observed lower quantum yield for motion (Fig. 4A).

In addition to the overall reduction in quantum yield, the threshold voltage for excitation appears to shift to higher energy with longer molecular length (Fig. 4A). This shift indicates that the Co atom at the fcc site experiences a higher potential barrier to transfer from the fcc to the hcp site. By directly comparing the energies of the linear and canted configurations (Fig. 1, A and B), DFT calculations once more provide an understanding of the atom motion. Figure 4B shows the variation in energy as the

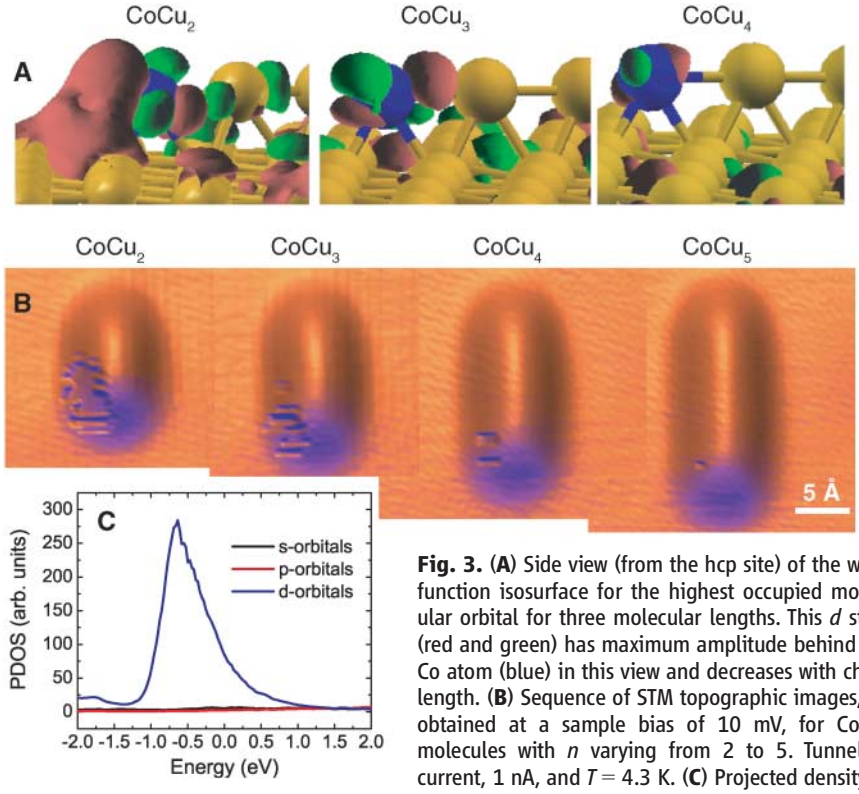

Fig. 3. (**A**) Side view (from the hcp site) of the wave function isosurface for the highest occupied molecular orbital for three molecular lengths. This *d* state (red and green) has maximum amplitude behind the Co atom (blue) in this view and decreases with chain length. (**B**) Sequence of STM topographic images, all obtained at a sample bias of 10 mV, for $CoCu_n$ molecules with *n* varying from 2 to 5. Tunneling current, 1 nA, and $T = 4.3$ K. (**C**) Projected density of states (PDOS, in arbitrary units) of Co in the $CoCu_2$ molecule on the Cu(111) surface.

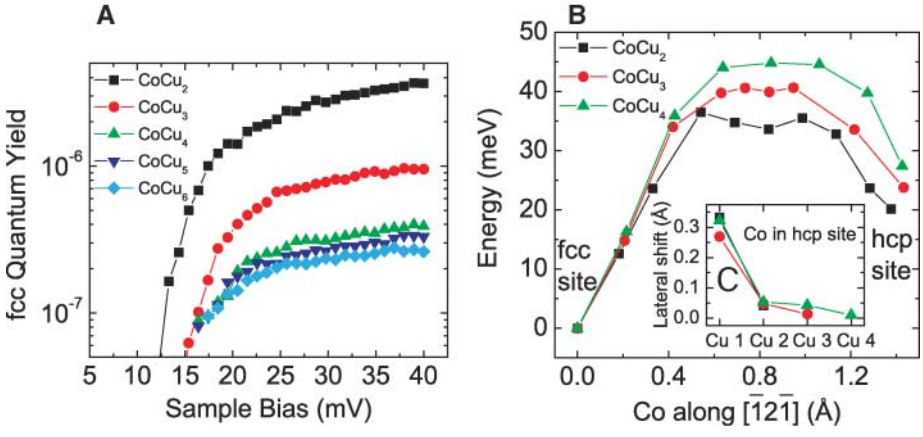

Fig. 4. (**A**) Fcc quantum yield for the Co atom for the various $CoCu_n$ molecules. (**B**) DFT calculations of the energy path for the Co moving from the fcc site (linear configuration) to the hcp site (canted configuration) for three molecular lengths. (**C**) The absolute value of the displacement of the Cu chain atoms with respect to their fcc position for the canted configuration.

Co atom moves from the fcc site to the hcp site for three molecular lengths. As the Cu chain increases, so does the energy difference between fcc and hcp sites and the energy barrier dividing them (Fig. 4B). These trends correspond to a stabilization of the linear configuration of the molecule and explain the experimental observation of increased stability of the fcc site as n increases (Figs. 3B and 4A). The motion of the Co atom becomes progressively hindered as the Cu chain length increases, because more atoms in the Cu chain must bend away from their energetically favored fcc positions, as is illustrated in Fig. 4C, where the resulting lateral shifts of the Cu chain atoms from their ideal positions are plotted for different chain lengths.

Because the smallest atomic-scale switch will likely involve modulating the electrical conductivity through the control of a single atom, the extension of studies such as this to semiconductor and insulating thin films could point the way to new classes of atomic-scale electronic and magnetic devices.

References and Notes

1. D. M. Eigler, E. K. Schweizer, *Nature* **344**, 524 (1990).
2. J. A. Stroscio, D. M. Eigler, *Science* **254**, 1319 (1991).
3. L. Bartels, G. Meyer, K.-H. Rieder, *Phys. Rev. Lett.* **79**, 697 (1997).
4. D. M. Eigler, C. P. Lutz, W. E. Rudge, *Nature* **352**, 600 (1991).
5. B. C. Stipe, M. A. Rezaei, W. Ho, *Science* **279**, 1907 (1998).
6. T. Komeda, Y. Kim, M. Kawai, B. N. J. Persson, H. Ueba, *Science* **295**, 2055 (2002).
7. A. J. Heinrich, C. P. Lutz, J. A. Gupta, D. M. Eigler, *Science* **298**, 1381 (2002); published online 24 October 2002 (10.1126/science.1076768).
8. W. Ho, *J. Chem. Phys.* **117**, 11033 (2002).
9. J. I. Pascual *et al.*, *Nature* **423**, 525 (2003).
10. J. A. Stroscio, R. J. Celotta, *Science* **306**, 242 (2004); published online 9 September 2004 (10.1126/science.1102370).
11. M. Lastapis *et al.*, *Science* **308**, 1000 (2005).
12. K.-Y. Kwon *et al.*, *Phys. Rev. Lett.* **95**, 166101 (2005).
13. Measurements were made in a cryogenic ultrahigh-vacuum STM instrument of our own design. We deposited Co and Cu atoms onto a Cu(111) surface, which was initially cleaned by ion sputtering and annealing. Co and Cu atoms can be chemically distinguished on the Cu(111) surface on the basis of STM spectroscopy measurements of the Co Kondo resonance. STM measurements were made by using Ir probe tips and a substrate temperature of 4.3 K.
14. B. N. J. Persson, A. Baratoff, *Phys. Rev. Lett.* **59**, 339 (1987).
15. J. W. Gadzuk, *Phys. Rev. B* **44**, 13466 (1991).
16. G. P. Salam, M. Persson, R. E. Palmer, *Phys. Rev. B* **49**, 10655 (1994).
17. S. Gao, M. Persson, B. I. Lundqvist, *Phys. Rev. B* **55**, 4825 (1997).
18. S. Fölsch, P. Hyldgaard, R. Koch, K. H. Ploog, *Phys. Rev. Lett.* **92**, 056803 (2004).

19. We thank S. Blankenship for technical assistance and are grateful for several fruitful discussions with J. W. Gadzuk, D. Penn, and M. Stiles. This work was supported in part by the Office of Naval Research.

Supporting Online Material
www.sciencemag.org/cgi/content/full/313/5789/948/DC1
Fig. S1

10 May 2006; accepted 11 July 2006
10.1126/science.1129788

Controlling the Electronic Structure of Bilayer Graphene

Taisuke Ohta,[1,2]* Aaron Bostwick,[1]* Thomas Seyller,[3] Karsten Horn,[2] Eli Rotenberg[1]†

We describe the synthesis of bilayer graphene thin films deposited on insulating silicon carbide and report the characterization of their electronic band structure using angle-resolved photoemission. By selectively adjusting the carrier concentration in each layer, changes in the Coulomb potential led to control of the gap between valence and conduction bands. This control over the band structure suggests the potential application of bilayer graphene to switching functions in atomic-scale electronic devices.

Carbon-based materials such as carbon nanotubes (CNTs), graphite intercalation compounds, fullerenes, and ultrathin graphite films exhibit many exotic phenomena such as superconductivity (*1*–*3*) and an anomalous quantum Hall effect (*4*–*6*). These findings have caused renewed interest in the electronic structure of ultrathin layers of graphite, such as graphene: a single hexagonal carbon layer that is the building block for these materials. There is a strong motivation to incorporate graphene multilayers into atomic-scale devices, spurred on by rapid progress in their fabrication and manipulation.

We studied the valence band (VB) structure of a bilayer of graphene and demonstrated that through selective control of the carrier concentration in the graphene layers, one can easily tune the band structure near the Dirac crossing. Similar control can be achieved in principle by varying the electric field across the bilayer film in an atomic-scale switching device.

The electronic states of graphene can be well described within basic calculational schemes (*7*–*9*). Graphene is a flat layer of carbon atoms arranged in a hexagonal lattice with two carbon atoms per unit cell. Of the four valence states, three sp^2 orbitals form a σ state with three neighboring carbon atoms, and one p orbital develops into delocalized π and π* states that form the highest occupied VB and the lowest unoccupied conduction band (CB). The π and π* states of graphene are degenerate at the corner (K point) of the hexagonal Brillouin zone (BZ) (Fig. 1A). This degeneracy occurs at the so-called Dirac crossing energy E_D, which at the normal half-filling condition coincides with the Fermi level (E_F), resulting in a pointlike metallic Fermi surface (Fig. 2E).

Strictly speaking, undoped graphene is a semimetal because although there is a state crossing at $E_D = E_F$, the density of states there is zero and conduction is possible only with thermally excited electrons at finite temperature. In applying an effective mass description for the VB and CB (*7*), one arrives at a formal equivalence between the resulting differential equation and the Dirac equation, hence charge carriers in the vicinity of E_F may be termed "Dirac fermions" (with the crossing point at K being named the Dirac point). Moreover, the particular band structure at the BZ boundary (that is, a linear dispersion) leads to an effective mass $m^* = 0$ at the point where the VB and CB meet. The peculiar band structure in ultrathin graphite layers results in a number of unusual electronic transport properties, such as an anomalous quantum Hall effect (*4*–*6*, *10*).

The graphene band structure is sensitive to the lattice symmetry. If the hexagonal layer structure is composed of nonequivalent elements, such as in boron nitride, the lateral, in-plane symmetry is broken, resulting in the formation of a large gap between π and π* states (*11*). The symmetry can also be broken with respect to the c axis by stacking two graphene layers in Bernal stacking (the stacking fashion of graphite) as suggested by McCann and Fal'ko (*12*) (Fig. 1B). Because the unit cell of a bilayer contains four atoms, its band structure acquires two additional bands, π and π* states, in each valley split by interlayer (A-B) coupling, and two lower energy bands. If the individual graphene layers in a bilayer are rendered inequivalent (Fig. 1C), then an energy gap between low-energy bands forms at the former Dirac crossing point (*12*). Provided that the charge state is such that E_F lies within the gap, a semimetal-to-insulator transition occurs. If this symmetry breaking could be controlled externally, the electronic conductivity would change through this transition, suggesting that a switch with a thickness of two atomic layers could be constructed.

To see whether this gedanken experiment can be realized, we synthesized bilayer graphene

[1]Advanced Light Source, Lawrence Berkeley National Laboratory, One Cyclotron Road, Berkeley, CA 94720, USA. [2]Department of Molecular Physics, Fritz-Haber-Institut, der Max-Planck-Gesellschaft, Faradayweg 4-6, D-14195 Berlin, Germany. [3]Institut für Physik der Kondensierten Materie, Universität Erlangen-Nürnberg, Erwin-Rommel-Strasse 1, D-91058 Erlangen, Germany.

*These authors contributed equally to this work.
†To whom correspondence should be addressed.